higher temperatures in the lower mantle would be smaller. The physical basis for this argument is weak, however, because the nature of LPO is closely related to the geometry of slip systems and of twinning which is sensitive to temperatures, and there is no general relation between LPO and temperatures. In fact, less LPO is found under lower temperatures in olivine because of the complexities of the active slip systems [A. Nicolas and N. I. Christensen, in *Composition, Structure and Dynamics of the Lithosphere/Asthenosphere System*, K. Fuchs and C. Froidevaux, Eds (American Geophysical Union, Washington, DC, 1987), pp. 111–123]. This trend in olivine is inconsistent with the observation of Meade *et al.* and suggests that mechanisms other than dislocation glide (for example, fracturing) are responsible for the LPO observed in these experiments.

17. Defect-related properties that control the preferred orientation of minerals include slip systems and twinning mechanisms [see, for example, P. van Houtte and F. Wagner, in *Preferred Orientation in Deformed Metals and Rocks: An Introduction to Modern Texture Analysis*, H.-R. Wenk, Ed. (Academic Press, New York, 1985), pp. 233–258], both of which are similar between $CaTiO_3$ and $(Mg,Fe)SiO_3$ [N. Doukhan and J.-C. Doukhan, *Phys. Chem. Mineral.* **13**, 403 (1986); S. Karato, K. Fujino, E. Ito, *Geophys. Res. Lett.* **17**, 13 (1990); Y. Wang, thesis, State University of New York at Stony Brook (1991), p. 232].
18. S. Karato and P. Li, *Science* **255**, 1238 (1992); P. Li, S. Karato, Z. Wang, *Phys. Earth Planet. Inter.*, in press.
19. S. Zhang and S. Karato, *Nature* **375**, 774 (1995).
20. Deformation in the lower mantle will be dominated by a vertical motion associated with upwelling or downgoing plumes except near the bottom (that is, the D″ layer) and a possible boundary layer near the 660 km discontinuity. Thus, the dominant mode of deformation in the lower mantle will be vertical shear to a first approximation.
21. At this *P-T* condition, $CaTiO_3$ assumes an orthorhombic structure (space group *Pbnm*) that is the same as the structure of the $(Mg,Fe)SiO_3$ perovskite under most lower mantle conditions (*10*). The homologous temperature (that is, T/T_m) in the lower mantle is similar to these conditions (T/T_m = 0.6 to 0.7 in the shallow lower mantle [A. Zerr and R. Boehler, *Science* **262**, 553 (1993)]. Under these conditions, a fine-grained (~8 μm) $CaTiO_3$ will deform by diffusion (or superplastic) creep, whereas a coarse-grained (~70 μm) counterpart will deform by dislocation creep (*18*).
22. G. S. Lister and A. W. Snoke, *J. Struct. Geol.* **6**, 617 (1984).
23. J. W. Edington, K. N. Melton, C. P. Cutler, *Prog. Mater. Sci.* **21**, 63 (1976).
24. X-ray measurements of the orientation of (040) lattice planes were made for both coarse- and fine-grained specimens in reflection and transmission geometry. In optical measurements for coarse-grained specimens, the preferred orientation of all of the three crystallographic axes of individual grains was determined with the universal stage. This is not possible to do for fine-grained specimens, so we measured the orientation of the {110} twin boundaries on the polished and etched sections. About 2000 twin boundaries were measured.
25. We used laboratory data on $MgSiO_3$ perovskite at ambient conditions. The effects of pressure and temperature on individual elastic constants in perovskite are not known, and neither are the effects of Fe, which might change the anisotropy. However, in the case of olivine, the temperature and pressure effects and also the effects of Fe on anisotropy are weak (*7*), so therefore we assume that the elastic anisotropy of perovskite in the lower mantle is similar to that measured at room pressure and temperature (*11*).
26. D. H. Mainprice, *Comput. Geosci.* **16**, 385 (1990). In this calculation, the elastic constants of a single crystal of $MgSiO_3$ perovskite are used, and the anisotropic elastic properties of an aggregate are calculated from the orientation of individual grains by using the Voigt averaging scheme.
27. Shear wave splitting was studied near subduction zones (*9*). Seismic tomography (*15*) and some numerical simulations [P. Tackley, D. J. Stevenson, G. A. Glazmaier, G. Schubert, *Nature* **361**, 699 (1993); S. Honda, D. A. Yuen, S. Balachandar, D. Reuteler, *Science* **259**, 1308 (1993)] suggest that the dominant geometry of deformation in these regions is vertical shear.
28. The seismic anisotropy for samples deformed by superplastic creep was not calculated because the complete crystallographic orientation of individual grains was measured only for coarse-grained samples deformed by dislocation creep. However, the nearly random orientation of grains found by x-ray measurements (Fig. 2) indicates that seismic anisotropy must be very weak.
29. E. Ito and H. Sato, *Nature* **351**, 140 (1991).
30. P. van Keken, D. A. Yuen, A. van den Berg, *Earth Planet. Sci. Lett.* **112**, 179 (1992); A. P. van den Berg, P. van Keken, D. A. Yuen, *Geophys. J. Int.* **115**, 62 (1993); P. van Keken, D. A. Yuen, A. van den Berg, *Geophys. Res. Lett.* **20**, 1927 (1993).
31. We thank P. G. Silver and D. A. Yuen for discussions and D. H. Mainprice for sending the program to calculate the seismic anisotropy. Supported by grants from NSF to S.K. (EAR-9206683 and EAR-9220172).

30 May 1995; accepted 11 August 1995

Large-Scale Interplanetary Magnetic Field Configuration Revealed by Solar Radio Bursts

M. J. Reiner, J. Fainberg, R. G. Stone

An instantaneous view of the interplanetary extension of the solar magnetic field is provided here by measurements from a space platform at high ecliptic latitudes of the trajectories of individual type III solar radio bursts. The Ulysses spacecraft provides this unique vantage point with an orbit taking it far from the ecliptic plane. The Ulysses radio measurements illustrate the capability of detecting and tracking coronal disturbances as they propagate through the interplanetary medium.

Solar energetic processes, such as solar flares, inject energetic electrons into interplanetary space, where, as a result of their small gyroradii, these electrons are constrained to follow the interplanetary extension of the solar magnetic field. As the suprathermal electrons propagate through the interplanetary medium, they interact with the local plasma to generate radio emissions (*1*) at the plasma frequency and its harmonic (*2*). Because the plasma frequency (proportional to the square root of the solar wind plasma density) falls off with increasing heliocentric distance, radio emission generated farther from the sun occurs at lower frequencies. For radio emission generated from regions near the sun to near Earth's orbit at 1 astronomical unit (1 AU = 1.5×10^8 km), the plasma frequency ranges from several hundreds of megahertz to ~50 kHz; the precise values depend on the interplanetary conditions at the time of the radio emission and on whether the emission occurs at the fundamental or harmonic of the plasma frequency. Both direct observations (*3, 4*) and modeling (*5*) indicate that the radio emission is broadly beamed in the direction of the interplanetary magnetic field, but the value of the beamwidth is difficult to estimate. The radio manifestation of the interaction of the electrons with the solar wind as they propagate along the magnetic field lines through the interplanetary medium is known as a type III radio burst (*6*). Low-frequency type III radio bursts have been observed for decades by spacecraft located in the ecliptic plane (*7*).

M. J. Reiner, Hughes STX, Lanham, MD 20706, USA.
J. Fainberg and R. G. Stone, NASA Goddard Space Flight Center, Greenbelt, MD 20771, USA.

The Ulysses spacecraft, launched in October 1990, used the intense gravitational field of Jupiter to rotate its orbital plane far out of the ecliptic; it became the first spacecraft to go to high ecliptic latitudes and over the poles of the sun (*8*). During the southern polar pass, which occurred during September and October of 1994, Ulysses went as high as 80°S ecliptic latitude at a distance of ~2 AU below the ecliptic plane. After a rapid passage through the ecliptic plane (~1° day^{-1} in ecliptic latitude), Ulysses made a northern polar pass, reaching a maximum northern ecliptic latitude of 79°N in late August 1995. The instrumentation on Ulysses includes a sensitive radio receiver (*9*) with 76 discrete frequency channels covering the range from 1 to 940 kHz. This receiver is coupled to a 72.5-m (tip to tip) dipole antenna in the spin plane of the spacecraft and a 7.5-m monopole antenna along the spacecraft spin axis. During the in-ecliptic phase of the Ulysses mission, thousands of type III radio bursts were observed by this instrument. The Ulysses radio experiment was designed to determine the direction of arrival of the radiation from the measured modulation in the radio signals as the spacecraft spins about its axis (*10*). Ulysses observations therefore permit tracking of type III radio sources through interplanetary space.

During its trajectory to high latitudes, Ulysses continued to observe type III radio emission (*11*). This observation is significant because solar active regions, from which the type III–generating suprathermal electrons originate, are generally confined to low solar latitudes [~10° north or south of the solar equator at solar minimum (*12*)]. It is therefore expected that the suprathermal electrons, and hence the type III radio sources, should be confined to relatively low-latitude interplanetary field lines. Indeed, evidence has been presented that most type III radio trajectories lie within 30° of the ecliptic plane (*13*). Because type III radio emission is beamed in the direction of the magnetic field, at sufficiently high latitudes the spacecraft may eventually move out of the beam pattern.

There are two possible reasons why type III radio bursts are observed at high latitudes: the latitudinal beamwidth is very broad or the radiation is scattered to high latitudes. A broad latitudinal beamwidth is suggested in analogy with estimates that the longitudinal beamwidth is greater than 100° (*5*); scattering is suggested since it is known to play an important role because of density inhomogeneities in the interplanetary medium near radio source regions (*4*).

The radio emission generated by the interaction of the suprathermal electrons with the solar wind produces frequency-drifting signatures in the measured dynamic spectrum (Fig. 1A). These are the identifying characteristics of type III radio bursts. During the 12-hour period of Fig. 1, at least four type III radio bursts were detected, with a particularly intense burst occurring at ~10:15 UT that extended from 940 kHz to below 30 kHz. The emission at high frequency (~940 kHz) corresponds to the radio source near (~0.1 AU) the sun; emission at low frequency (~63 kHz) corresponds to the radio source, and therefore the electrons, far (~1 AU) from the sun. Because of the large but finite speed of the exciter electrons [between 0.1*c* and 0.3*c* (*14*), where *c* is the speed of light in a vacuum], the onset of the radio emission occurs at progressively later times at lower frequencies, hence the observed frequency drift. At these speeds, it takes the exciter electrons about 20 min to travel from the sun to 1 AU. The duration of the radio emission increases with decreasing frequency from ~10 min at 940 kHz to ~1.5 hours at 63 kHz.

The type III intensity profiles (Fig. 1B) display no obvious differences from burst profiles previously observed from spacecraft located in the ecliptic plane (*7*); they consist of a rapid rise to a maximum intensity followed by a slower exponential-like decay. Ulysses has observed numerous type III radio bursts like those in Fig. 1 from high ecliptic latitudes.

We measured the direction of arrival of the radiation at each observing frequency for the intense burst in Fig. 1 beginning at 10:15 UT. This burst was associated with a solar flare at ~10:08 UT that occurred in an active region located at 6°S, 11°W on the solar surface as seen from Earth. Making the reasonable assumption that the radio sources originating from this flare site remain close to the ecliptic plane, the intersections of the arrival directions with the ecliptic plane at each frequency (Fig. 2) should approximate the radio trajectory through interplanetary space for this type III burst. The type III radio trajectory which represents the average path followed by the suprathermal exciter electrons follows a spiral-like path corresponding to heliocentric distances from ~0.1 to 0.8 AU, in close approximation to a 400-km s^{-1} Archimedean spiral (solid blue curve). Deviations from the Archimedean spiral path result from temporal variations in the interplanetary plasma, which distort the spiral field lines, and from small errors in the observed radio source directions. Because of the unique perspective of these observations, any inclination of the actual radio trajectory above or below the ecliptic plane would not alter the spiral characteristic; it would imply only a different solar wind speed.

Five days later, at about 13:35 UT on 30 October 1994, Ulysses observed another intense type III radio burst. This burst was not associated with an observed solar flare, but there was an active region on the sun at 18°N, 13°E (relative to Earth) that may have been the origin of the energetic electrons. This radio trajectory also followed a spiral-like path (Fig. 2), this time corresponding to a solar wind speed of ~300 km s^{-1} (dashed blue curve). The radio source locations shown range in frequency from 940 to 81 kHz, corresponding to heliocentric distances from 0.1 to 1.1 AU, suggesting that the interplanetary density along the 30 October trajectory was somewhat higher than that along the 25 October trajectory; this reflects different interplanetary conditions encountered at these two locations and time periods. This burst illustrates the advantage of tracking type III radio bursts far from the ecliptic plane. From the location of Ulysses at high ecliptic latitudes, radio bursts originating from any solar longitude can be clearly viewed and tracked through interplanetary space. By contrast, from the perspective of an observer near

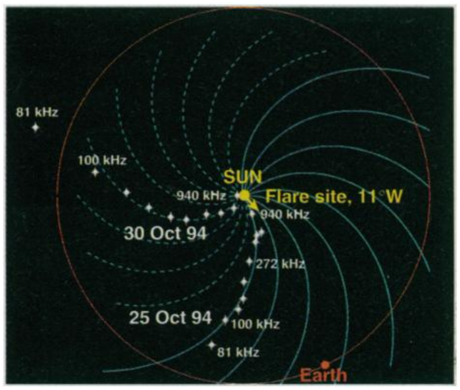

Fig. 2. A view of the ecliptic plane from the northern ecliptic pole, showing measured radio trajectories for two type III radio bursts observed by Ulysses on 25 and 30 October 1994 from ~2 AU above the south solar pole. Both trajectories follow spiral-like paths through interplanetary space from near the sun to ~1 AU. The stars correspond to the radio source locations at 10 discrete observing frequencies extending from 940 to 81 kHz. The blue curves are Archimedean (Parker) spirals corresponding to solar wind speeds of 300 km s^{-1} (dashed curves) and 400 km s^{-1} (solid curves). The flare site for the 25 October event, relative to the corresponding trajectory and to the location of the Earth, is also indicated.

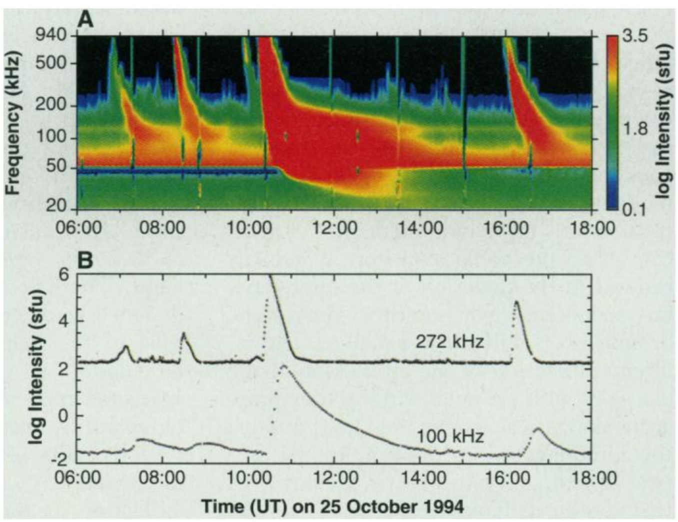

Fig. 1. (**A**) Dynamic spectral representation of the Ulysses radio data from 06:00 to 18:00 UT (universal time at the spacecraft) on 25 October 1994, showing four frequency-drifting type III radio bursts observed by Ulysses from 78°S ecliptic latitude (74°S heliographic latitude). The color scale shows the intensity in solar flux units (sfu) (1 sfu = 10^{-22} W m^{-2} Hz^{-1}). The horizontal band at about 50 kHz is an artifact of the transition between two different radio receivers. (**B**) Intensity versus time plots for two discrete frequency channels showing the profiles of the type III radio bursts in (A). The profile for 100 kHz was downshifted by 4 units for clarity of presentation.

Earth, this burst would be difficult to track because of both the foreshortening of the spiral path and the passage of the burst around the east limb of the sun.

Because the entire radio trajectory, and therefore the underlying magnetic field structure, from the sun to ~1 AU was measured in less than 1 hour, the measured radio trajectories provide an essentially instantaneous visualization of the spiral magnetic field configuration. Figure 2 represents a radio "snapshot" taken by Ulysses from high ecliptic latitudes of conditions in the solar wind near the ecliptic plane during the time of these bursts. From the measured path lengths followed by the exciter electrons along the radio trajectories in Fig. 2 and from the measured onset times of the radio emission at different frequencies determined from the burst profiles (such as shown in Fig. 1B), we find that the average exciter speed for both bursts lies between 0.3*c* and 0.4*c*, which is consistent with more energetic exciters previously reported (*14*).

The results in Fig. 2 can be understood in terms of Parker's (*15*) prediction that the interplanetary extension of the solar coronal magnetic field is wound into Archimedean spirals because of the rotation of the sun and the radial outflow of the solar wind. The curvature of the spiral is fixed by the solar wind speed; a slow solar wind speed corresponds to a more tightly wound spiral. The average spiral structure of the coronal magnetic fields has since been confirmed by numerous in situ spacecraft measurements of the average angle of the magnetic field vector (*16*). Such single point measurements, however, do not reveal the instantaneous spiral structure out to 1 AU. The Ulysses radio observations provide a direct unequivocal confirmation of Parker's 1958 prediction of the interplanetary magnetic field topology under quiet solar wind conditions.

Tracking of individual type III radio bursts from spacecraft located in the ecliptic plane was previously used to derive an instantaneous picture of the average spiral magnetic field topology from the sun to 1 AU (*17*). The radio trajectories derived by this method were often difficult to obtain because, in addition to limb effects and the foreshortening of the interplanetary field lines for an observer in the ecliptic plane, it was necessary to assume an average interplanetary density-distance scale. The determination of the radio burst trajectories was very sensitive to the relation between the electron plasma density and radial distance from the sun, which is only an average approximation and does not take into account the large temporal variations in solar wind velocity and density. Nevertheless, Fainberg, Evans, and Stone used IMP-6 (Interplanetary Monitoring Platform) radio data to trace the global spiral magnetic field configuration from the sun to 1 AU (*18*); such observations provided the first indirect observation of the global spiral structure of interplanetary magnetic fields. By contrast, no assumptions had to be made about a density-distance scale in our determination of the radio source locations (*19*).

Another problem affecting observations made by spacecraft near the ecliptic is that scattering and refraction of radio waves by density inhomogeneities and possibly associated anomalous time delays (*4*) can significantly alter derived trajectories and exciter speeds. Because the interplanetary plasma is less dense and more homogeneous at high latitudes (*20*), the Ulysses radio observations are affected much less by propagation anomalies.

From the unique perspective of Ulysses at high latitudes, type III radio trajectories can also be used to determine the magnetic configuration in the disturbed solar wind when field lines deviate significantly from the Parker spiral. The radio trajectory for an intense type III radio burst that occurred at 20:30 UT on 26 November (Fig. 3) deviated significantly from an Archimedean spiral. There was a sudden change in direction of the radio trajectory between 740 and 272 kHz. It may have resulted from a transient disturbance propagating through the interplanetary medium. This interpretation is reinforced when we superpose on this plot a radio trajectory for another very intense radio burst, associated with a flare from the same active region (16°S, 10°W), that occurred on the following day, 27 November, at ~16:25 UT. The shape of this latter radio trajectory is similar to the 26 November trajectory, except that the sudden change in direction is observed at lower frequencies, between 196 and 148 kHz, which corresponds to a heliocentric distance about 0.3 AU farther from the sun than for the 26 November burst. A distance of 0.3 AU in one day corresponds to a structure propagating outward through the interplanetary medium at ~600 km s^{-1}, which is a typical speed for a transient interplanetary disturbance. These observations illustrate the potential for tracking transient interplanetary disturbances with type III radio bursts as tracers of the large-scale configuration of the interplanetary magnetic field.

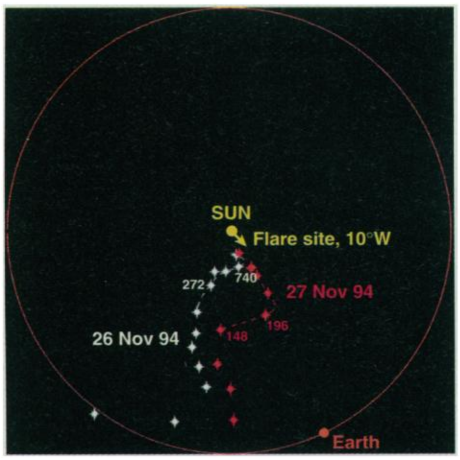

Fig. 3. A view of the ecliptic plane from the northern ecliptic pole, showing measured radio trajectories for two type III radio bursts observed by Ulysses on 26 and 27 November 1994 from 68°S ecliptic (62°S heliographic) latitude and ~1.8 AU from the sun. The second trajectory is rotated by ~14.4° to take into account the rotation of the sun during this time interval. The numbers near the points refer to the frequency (in kilohertz) at that point. The radio source locations for the 26 November event are shown at discrete frequencies ranging from 940 to 52 kHz, and for the 27 November event, ranging from 940 to 81 kHz. These trajectories follow paths that deviate significantly from an Archimedean spiral. They may indicate the presence of a transient interplanetary disturbance propagating outward through the interplanetary medium.

REFERENCES AND NOTES

1. J. P. Wild, *Aust. J. Sci. Res. Ser. A* **3**, 541 (1950).
2. ———, J. D. Murray, W. C. Rowe, *Aust. J. Phys.* **7**, 439 (1954); F. T. Haddock and H. Alvarez, *Sol. Phys.* **29**, 183 (1973); G. A Dulk, J. L. Steinberg, S. Hoang, *Astron. Astrophys.* **141**, 30 (1984); M. J. Reiner, R. G. Stone, J. Fainberg, *Astrophys. J.* **394**, 340 (1992).
3. R. J. Fitzenreiter, J. Fainberg, R. B. Bundy, *Sol. Phys.* **46**, 465 (1976).
4. J.-L. Steinberg *et al.*, *Astron. Astrophys.* **140**, 39 (1984).
5. M. J. Reiner and R. G. Stone, *ibid.* **217**, 251 (1989).
6. J. P. Wild and L. L. McCready, *Aust. J. Sci. Res. Ser. A* **3**, 387 (1950).
7. J. Fainberg and R. G. Stone, *Space Sci. Rev.* **16**, 145 (1974).
8. E. J. Smith, R. G. Marsden, D. E. Page, *Science* **268**, 1005 (1995).
9. R. G. Stone *et al.*, *Astron. Astrophys. Suppl. Ser.* **92**, 291(1992).
10. R. Manning and J. Fainberg, *Space Sci. Instrum.* **5**, 161 (1980).
11. R. G. Stone *et al.*, *Science* **268**, 1026 (1995).
12. E. W. Maunder, *Mon. Not. R. Astron. Soc.* **82**, 534 (1922).
13. G. A. Dulk *et al.*, in *The Sun and the Heliosphere in Three Dimensions*, R. G. Marsden, Ed. (Reidel, Dordrecht, Netherlands, 1986), pp. 229–233.
14. J. Fainberg and R. G. Stone, *Sol. Phys.* **15**, 433 (1970); G. A Dulk, J. L. Steinberg, S. Hoang, M. V. Goldman, *Astron. Astrophys.* **173**, 366 (1987).
15. E. N. Parker, *Astrophys. J.* **128**, 664 (1958).
16. J. M. Wilcox, *Science* **152**, 161 (1966).
17. J. Fainberg, L. G. Evans, R. G. Stone, *ibid.* **178**, 743 (1972).
18. Other techniques for deriving individual type III radio trajectories from spacecraft observations in the ecliptic plane have been developed [M. J. Reiner and R. G. Stone, *Sol. Phys.* **106**, 397 (1986); *Astron. Astrophys.* **206**, 316 (1988)]. These methods did not require a global density-distance scale; however, other assumptions had to be introduced to derive the radio trajectories. For periods of continuous radio emission observed during interplanetary type III radio storms, J.-L. Bougeret, J. Fainberg, and R. G. Stone [*Astron. Astrophys.* **141**, 17 (1984); *Science* **222**, 506 (1983)] derived radio trajectories out to ~0.7 AU without assuming a density-distance scale. In this case, the resulting spiral path represents an average of the interplanetary magnetic field configuration over several days. By contrast, tracking individual radio bursts provides a

picture of the field configuration over a much shorter time period (~1 hour).
19. From the measured positions in Fig. 2, a density-distance scale that does not differ significantly from that used earlier (7) can be derived; an approximate r^{-2} falloff (r is heliocentric distance) is indicated. These results reinforce the interpretation that the radiation observed by Ulysses occurs at the harmonic of the plasma frequency.
20. J. L. Phillips *et al.*, *Science* **268**, 1030 (1995).
21. We thank R. F. Benson for many useful suggestions for improving the manuscript.

4 August 1995; accepted 14 September 1995

Role of Yeast Insulin-Degrading Enzyme Homologs in Propheromone Processing and Bud Site Selection

Neil Adames, Kelly Blundell, Matthew N. Ashby, Charles Boone*

The *Saccharomyces cerevisiae AXL1* gene product Axl1p shares homology with the insulin-degrading enzyme family of endoproteases. Yeast *axl1* mutants showed a defect in **a**-factor pheromone secretion, and a probable site of processing by Axl1p was identified within the **a**-factor precursor. In addition, Axl1p appears to function as a morphogenetic determinant for axial bud site selection. Amino acid substitutions within the presumptive active site of Axl1p caused defects in propheromone processing but failed to perturb bud site selection. Thus, Axl1p has been shown to participate in the dual regulation of distinct signaling pathways, and a member of the insulinase family has been implicated in propeptide processing.

Peptide hormones secreted by higher eukaryotes are synthesized as larger precursors and released in mature form by the action of specific processing proteases (*1*). Analogous proteolytic maturation occurs for *Saccharomyces cerevisiae* pheromones involved in the mating response of haploid **a** and α cells (*2*). The pheromone produced by **a** cells, **a**-factor, is one of a growing number of secreted proteins, such as interleukin-1α (IL-1α), IL-1β, and some fibroblast growth factors (such as FGF-1 and FGF-2) (*3*), that are processed from precursors before export through a nonclassical secretory pathway. The proteolytic maturation of progenitor **a**-factor (pro–**a**-factor) is not well understood and provides an opportunity to identify novel eukaryotic processing enzymes. Here we present genetic evidence implicating yeast homologs of human insulin-degrading enzyme (hIDE), encoded by *AXL1* and *STE23*, in the specific processing of pro–**a**-factor.

Pro–**a**-factor is encoded by two genes, *MFA1* and *MFA2*, with products that are 36 and 38 amino acids in length, respectively (*4, 5*). These precursors contain a single copy of the mature **a**-factor peptide, with an NH_2-terminal extension and a COOH-terminal CAAX consensus sequence (C is cysteine, A is usually aliphatic, and X can be various amino acids). The cysteine residue of CAAX proteins is isoprenylated within the cytoplasm; such lipid-modified proteins become localized in the membrane, then undergo endoproteolysis of the three terminal AAX residues and methylesterification of the free carboxylate group on the prenylated cysteine (*6*). The genes encoding most of the enzymes responsible for these modifications have been characterized (*7, 8*), and mutations in these genes abolish **a**-factor secretion, leading to an **a**-specific mating defect (*7, 8*). After COOH-terminal processing, the **a**-factor precursor undergoes two sequential NH_2-terminal endoproteolytic events (*8, 9*). The final NH_2-terminal cleavage generates mature **a**-factor, a 12–amino acid lipopeptide (*10, 11*). Ultimately, the *STE6* product, an adenosine triphosphate–hydrolyzing transport protein related to the mammalian multidrug resistance protein (Mdr1), mediates **a**-factor transport across the cell surface (*12*).

To identify genes required for pro–**a**-factor maturation, we mutagenized **a** cells and screened for strains that showed a reduced mating efficiency as well as a defect in secreted **a**-factor activity (*13*). A mutant allele, designated *ste22-1*, identified a novel gene required for normal amounts of secreted **a**-factor activity (Fig. 1A). In crosses to a wild-type α strain, we found that the sterility cosegregated with this reduced pheromone production and that α *ste22-1* cells mated with normal efficiency (Fig. 1A). A similar but more severe **a**-specific phenotype was associated with a strain from which the **a**-factor structural genes *MFA1* and *MFA2* were deleted (Fig. 1A). Thus, *ste22-1* mutants exhibited an **a**-specific mating defect that appeared to be caused by reduced secretion of active pheromone.

We cloned *STE22* by complementation of the mating defect of *ste22-1* cells, using a yeast genomic library. Four plasmids, with overlapping genomic inserts, that complemented both the sterility and the reduced **a**-factor production were isolated. Subcloning and sequence analysis revealed that *STE22* was identical to *AXL1* (*14*). Thus, *AXL1* rescued the mating defect of *ste22-1* cells (Fig. 1B). The *AXL1* product is required for generation of the axial budding pattern displayed by haploid cells (*14*) and shares sequence similarity with members of a family of endoproteases whose archetypes are hIDE and *Escherichia coli* protease III (*15*)–metalloproteases with a preference for small peptide substrates (*16, 17*). In vivo, hIDE is implicated in the degradation of intracellular insulin, whereas the physiological substrate of protease III remains unknown (*16, 17*). Another member of the hIDE family, rat *N*-arginine dibasic convertase (NRDC), is proposed to function as a prohormone processing enzyme (*18*). A highly conserved domain is present in hIDE-like sequences that is likely to be important both for proteolysis and for metal binding (Fig. 2A) (*17*).

An *axl1::URA3* disruption was constructed (Fig. 2B) and introduced into a diploid strain that was heterozygous for *ste22-1*. Sporulation and tetrad analysis revealed that *axl1::URA3* was tightly linked to *ste22-1* (*19*). Moreover, the *axl1::URA3* phenotype was comparable to that of *ste22-1* (Fig. 1A). These data confirmed that *ste22-1* was a mutant allele of *AXL1*. Mutations in *AXL1* cause haploid cells to bud with a bipolar pattern that is normally displayed by diploid cells (*14*). Because the genetic background of the strain we used for the mutant isolation is defective for bud site selection (*20*), we constructed an *axl1* disruption in a haploid strain normal for axial budding, EG123. This *axl1::URA3* mutant showed both a bipolar budding pattern and a mating defect associated with reduced **a**-factor secretion (*19*).

Because insulinase homologs can function as specific endoproteases (*18*), Axl1p may act as a propheromone processing enzyme. We tested an *axl1* mutant for defects in COOH-terminal CAAX-proteolysis and found it to be unaffected (*21*). To address the possibility that Axl1p is involved in NH_2-terminal processing, **a**-factor proteins were labeled with [^{35}S]cysteine in a pulse-chase protocol, then immunoprecipitated from both intracellular and extracellular fractions and subjected to polyacrylamide gel electrophoresis (PAGE). Three different intracellular **a**-factor peptides were observed in cells containing a functional

N. Adames, K. Blundell, C. Boone, Institute of Molecular Biology and Biochemistry, Simon Fraser University, Burnaby, British Columbia, V5A 1S6, Canada.
M. N. Ashby, Department of Molecular and Cell Biology, University of California, Berkeley, CA 94720, USA.

*To whom correspondence should be addressed.